

Steady increase in geomagnetic reversal frequency after the Cretaceous Normal Superchron

Yutaka Yoshimura (✉ yoshimura.yutaka.36w@kyoto-u.jp)

Kyushu University <https://orcid.org/0000-0003-2850-4975>

Osamu Ishizuka

Geological Survey of Japan/AIST

Toshitsugu Yamazaki

University of Tokyo <https://orcid.org/0000-0003-2818-8335>

Yuhji Yamamoto

Kochi University

Hyeon-Seon Ahn

Korea Institute of Geoscience and Mineral Resources (KIGAM)

Tesfaye Kidane

Addis Ababa University

Yo-ichiro Otofujii

Kobe University <https://orcid.org/0000-0002-0594-7821>

Shun Sekimoto

Institute for Integrated Radiation and Nuclear Science, Kyoto University

Article

Keywords:

Posted Date: January 13th, 2022

DOI: <https://doi.org/10.21203/rs.3.rs-1186868/v1>

License:   This work is licensed under a Creative Commons Attribution 4.0 International License.

[Read Full License](#)

Abstract

The Earth's core is constantly and efficiently cooled by mantle convection. The heat flux transferred from the core to the mantle through the core-mantle boundary (CMB) is critical for understanding the dynamics of solid Earth. Although it is difficult to estimate the CMB heat flux, its history could be reconstructed from geomagnetic reversal frequency. However, overlooked short geomagnetic reversals may exist in the geomagnetic polarity time scale (GPTS), which affects the estimation of the heat flux history. Here, we report four new high-precision $^{40}\text{Ar}/^{39}\text{Ar}$ ages of the Oligocene Ethiopian traps. The traps may contain undiscovered reversals in marine magnetic anomaly. Based on the ages, we identified new reversals in Chron C12n, which was not found in marine magnetic anomalies. Our non-parametric analysis of GPTS suggests four potential periods of missing geomagnetic reversals, which correspond to long polarity intervals in GPTS. We found that C12n correspond to one of the periods. This indicates that several undetected reversals may exist within or near the edge of long polarity intervals after the Cretaceous Normal Superchron (prolonged stable polarity period). Considering the undetected reversals, we conclude that the CMB heat flux increased more slowly and monotonically after the Superchron than that ever estimated.

Main

Heat flux transferred from the core to the mantle through the core-mantle boundary (CMB) is important for understanding the dynamics of solid earth. The current estimate of the CMB heat flux is uncertain, at 5–15 terawatts¹. Based on numerical geodynamo simulations, the geomagnetic reversal frequency can be a proxy for the changes in the heat flux at CMB on scales of tens of millions of years². The geomagnetic polarity time scale (GPTS), which is the basis for calculating the geomagnetic reversal frequency, has been refined continuously³. However, short geomagnetic reversals might still be overlooked in GPTS^{4,5}. Therefore, in this study, we focused on the age of the Oligocene Ethiopian traps which might contain undiscovered geomagnetic reversals in marine magnetic anomaly⁶.

The Oligocene Ethiopian traps are one of the three volcanic pulses of the Afro-Arabian Large Igneous Province from the Eocene to Miocene⁷. At the Lima-Limo section of the Ethiopian traps (Fig. 1a), several studies on palaeomagnetism and $^{40}\text{Ar}/^{39}\text{Ar}$ age have estimated that its eruption duration is 1.5 million years or less (Myr)^{6,8–10}. However, in previous studies, a unique age correlation was not found using magnetostratigraphy (Fig. 1b). Recently, seven magnetozones were identified from the traps: R1–N1–R2–N2–R3–N3–R4, from the bottom to the top of the section⁶. Six geomagnetic reversals recorded in the traps with the estimated duration of the volcanism of 0.9 Myr⁶ indicate that the geomagnetic reversal frequency for this period (6.7/Myr) is 2.5 times higher than the reversal frequency estimated for 30 Myr ago (Ma) (2.7/Myr)¹¹. This discrepancy suggests that the duration may be incorrect or that it may contain geomagnetic reversals that have not been discovered on the Geomagnetic Polarity Time Scale (GPTS). In order to resolve the discrepancy, it is necessary to establish a unique correlation between GPTS and the Lima-Limo section using new radioisotopic ages.

$^{40}\text{Ar}/^{39}\text{Ar}$ dating of the Oligocene Ethiopian traps

We conducted four high-precision $^{40}\text{Ar}/^{39}\text{Ar}$ datings¹² (see Methods). We used the same samples as previous palaeomagnetic studies^{6,13}. Before the dating experiments, we selected samples by inspecting thin sections (Fig. S1) to avoid contamination from secondary minerals. Samples A1–61 and A2–162 are from two reversely magnetized lava flows belonging to the R4 magnetozone. Samples A2–482 and A2–604 are from the normally magnetized lava flows belonging to N3 and N1 magnetozone, respectively. Four samples were dated by stepwise heating analysis (Table 1, S1; Fig. 2). Two samples (A1–61 and A2–162) yielded well-defined age plateaus comprised of 82.7% and 82.1% of released gas, respectively (Table 1, S1; Fig. 2). The inverse isochron ages for the two age spectra are identical to the weighted average ages of plateau-forming steps within 2σ error (Table 1; Fig. S2). These data indicate that the two plateau ages (29.63 ± 0.14 Ma for sample A1–61 and 30.02 ± 0.22 Ma for sample A2–162) (2σ , respectively) are reliable eruption ages of the basalts. A2–482 showed a partially disturbed age spectrum comprised of 44.9% of released gas and did not have a plateau in a strict mean (Table 1, S1; Fig. 2). However, the inverse isochron age of sample A2–482 (Fig. S2) is identical to the weighted average age of the middle-temperature steps and the $^{40}\text{Ar}/^{36}\text{Ar}$ intercept of the inverse isochron is consistent with the atmospheric ratio within 2σ error. Thus, the middle-temperature steps are regarded as plateau-forming steps, and the weighted average age (30.87 ± 0.22 Ma, 2σ) from these steps is interpreted as a reliable eruption age. Sample A2–604 gave an age spectrum comprised of 43.5% of the released gas and did not have a plateau in a strict mean either (Table 1, S1; Fig. 2). The age spectrum includes some apparent disturbance in low-temperature steps due to ^{39}Ar recoil in possible secondary phases. However, middle to high-temperature steps overlap with the plateau-forming steps of sample A2–162, which has a similar Ca/K plot with sample A2–604 (Fig. 2). These steps gave a weighted average age of 31.02 ± 0.24 Ma (2σ), which we interpret as plateau-forming steps and a reliable eruption age. Also, the four plateau ages are consistent with the altitudes in the Lima-Limo section (Fig. 3), which supports the reliability of the ages.

Age correlation with the geomagnetic polarity time scale

The new ages enable a unique correlation of the magnetostratigraphy to the GPTS2020³. GPTS2020 is the latest version of the geomagnetic polarity time scale. This GPTS provides ages of geomagnetic reversal boundaries based on marine magnetic anomalies since middle Mesozoic, which is constrained by astronomical tuning. Our four $^{40}\text{Ar}/^{39}\text{Ar}$ ages are calibrated using the FCs standard with the age of 28.201 Ma¹⁴ and the ^{40}K decay constant¹⁵, which are used in GPTS2020. Our ages are consistent with the previously reported high-precise ages from sanidine⁹ (Fig. S3). The age of sample A1–61 from the R4 magnetozone (29.82 ± 0.14 Ma, 2σ) corresponds to late Chron C11n.2n of GPTS2020 (Fig. 3). The correlation is inconsistent with the measured reversed polarity of the samples. However, we interpret that the sample A1–61 belongs to Chron C11r because the age of sample A1–61 is closer to that of the top of Chron C11r than the bottom of Chron C11n.1r (Fig. 3). On the other hand, the 2σ error range of the age of sample A2–162 (30.21 ± 0.22 Ma, 2σ) is close to the interval of Chron C11r (Fig. 3).

From these observations, the magnetozone R4 is considered to correspond to Chron C11r. The age of sample A2–482 from the N3 magnetozone (30.87 ± 0.22 Ma, 2σ) correspond to Chron C12n (Fig. 3). The age of sample A2–604 from the N1 magnetozone (31.02 ± 0.24 Ma, 2σ) correspond to late Chron C12r (Fig. 3). However, we consider that the N1 magnetozone also belongs to Chron C12n because C12n is only one correlative normal polarity (Chron C12n) near the age of sample A2–604. Samples A2–482 and A2–604 produced indistinguishable plateau ages within 2σ error, respectively (Fig. 3). Hence, we interpret that the magnetozones from N1 to N3 are within Chron C12n, and the R1 magnetozone is correlative to Chron C12r. In summary, we conclude the magnetostratigraphic correlation of the Lima-Limo section as C12r (R1)–C12n (N1-to-N3)–C11r (R4), with R2, N2, and R3 as short polarity intervals within C12n (Fig. 1b).

The three putative excursions in the R4 magnetozone and the one in the R1 magnetozone have been previously reported⁶ within Chrons C11r and C12r, respectively (Fig. 3) based on the VGP cut-off method¹⁶. These intermediate palaeomagnetic directions may be correlative with Cryptochron C11r-1 and one of eight Cryptochrons (C12r-8 to C12r-1) in Chron C12r, respectively (Cryptochrons were defined by Cande and Kent (17)). We tentatively assigned the age 29.97 Ma to the top of the magnetostratigraphy, which is the youngest age of Chron C11r, and 31.29 Ma to the bottom, which is the age of Cryptochron C12r-1 interpolated in GPTS2020 (Fig. 1b).

Based on our age constraints, four new reversals bounding the magnetozones from N1 to R3 are included in Chron C12n. We call these four brief reversals in Chron C12n “Lima-Limo reversals”, which are not identified from the marine magnetic anomalies¹⁷. A low of the relative palaeomagnetic intensity in the early C12n observed in Oligocene marine sediments^{18,19} may reflect the Lima-Limo reversals and suggest that this is a global event.

Geomagnetic reversal frequency estimation and missing reversals

Geomagnetic reversal is a stochastic phenomenon called Poisson process²⁰. Therefore, the Kernel Density Estimation (KDE), which is a sum of probability functions, is suitable to express the change in the geomagnetic reversal frequency. We used the fixed and locally adaptive KDE²¹ to estimate reversal frequency changes (see Methods). In general, the fixed KDE is expressed as the sum of Gaussian functions and depends on the bandwidth, which determines the standard deviation of the averages of the Gaussian functions. The bandwidth is optimised across the entire data set. As a result, the bandwidth may partly be too wide to extract short-wavelength features, while apparent features may be generated when the bandwidth is too narrow. On the other hand, the locally adaptive KDE optimises bandwidth in accordance with data by minimising the difference between true unknown rates and estimated rates assuming the Poisson processes. Therefore, the locally adaptive KDE can reveal true features of the reversal frequency changes. The curve of the fixed KDE has four reversal frequency minima after the Cretaceous Normal Superchron (CNS) (Fig. 4a, blue line, Table S2). However, a single peak and no minima (Fig. 4b, blue line, Table S2) is a true feature according to the locally adaptive KDE. This variation between 84 and 24 Ma is consistent with that estimated by a previous study¹¹ (Fig. 4b, gray line).

Therefore, the short-wavelength changes in the reversal frequency expressed by the fixed KDE could be artefacts. These apparent minima correspond to polarity chrons longer than 0.9 Myr in GPTS2020. However, true reversal frequency based on the locally adaptive KDE shows monotonical changes even during such periods. This discrepancy can be resolved if undiscovered geomagnetic reversals exist within or near the edges of these long chrons.

Next, we examined the change of reversal frequency curves when the Lima-Limo reversals were added to GPTS2020. For the fixed KDE, after adding the Lima-Limo reversals, the decrease of the reversal frequency curve at around 30 Ma became smaller (Fig. 4a, red line, Table S2) and closer to that of the locally adaptive KDE mentioned below. These observations means that the Lima-Limo reversals compensate the part of reversals undetected in marine magnetic anomalies. For the locally adaptive KDE, the addition of the Lima-Limo reversals resulted in a slight decrease in the curvature of the reversal frequency curve from 50 to 25 Ma (Fig. 4b, red line, Table S2). The rate of the reversal frequency increase is 0.12 Myr^{-1} and 0.10 Myr^{-1} from 40 to 25 Ma before and after adding the Lima-Limo reversals, respectively, which implies that the increasing rate of the reversal frequency after CNS is gradual and close to constant. The bend of the reversal frequency curve around 45 Ma (Fig. 4b, red line) may be an artefact due to the undetected geomagnetic reversals.

CMB heat flux change after CNS

The slow and monotonous increase in the reversal frequency after CNS suggests continuous and steady changes in the CMB heat flux after CNS. This is because the reversal frequency reflects the variations of the CMB heat flux average according to the numerical geodynamo simulations². A previous study linked reversal frequency to the growth and collapse of superplumes²². They interpreted the decrease in the reversal frequency as a collapse of a superplume. The collapse would trigger the production of hot plumes, and which leads the emplacement of the Large Igneous Provinces (LIPs) with a time lag of 30-60 Myr required for the hot plume to rise²². In other words, the timing of the emplacements of LIPs corresponds with the peaks of the reversal frequency with the time lag. However, over the past 160 Myr, our analysis shows that the reversal frequency had only three peaks, while LIPs have occurred nine times (Fig. 4b, c). Therefore, the change in the reversal frequency is alternatively interpreted to be linked with constant subduction and the fall of slabs onto the CMB, and not with sporadic superplume and activity of the LIPs. Based on this interpretation, the slow and monotonic increase in reversal frequency from 84 to 9.6 Ma suggests a gradual increase in the number of slabs reaching the CMB during this period. When further undetected geomagnetic reversals after CNS are discovered, the change in the reversal frequency during this period will become more gradual. Considering the observed time lag of 120 Myr between the subduction flux and the reversal frequency²³, the reversal frequency after CNS would therefore be a constraint for plate reconstruction models from ~220 to ~120 Ma.

Declarations

Acknowledgements

We appreciate Catherine Constable for providing the reversal frequency data. We thank Yusuke Suganuma, Kenichiro Tani, and Masakazu Fujii for their helpful discussions, suggestions, and information. We used thin sections made by Takashi Goto. We utilized the ALOS World 3D - 30m data of the “Daichi” (ALOS) satellite provided by JAXA for our sampling map and the “TopoUSM” (<https://github.com/geogin/TopoUSM-QGIS>) that is the plug-in of QGIS invented by Fumihiko Ikegami. Hironao Matsumoto helped with access to the GPTS2020 paper. We prepared groundmass grains using the SELFRAG Lab system at the National Museum of Nature and Science, Tsukuba. We also acknowledge Hideaki Shimazaki and Hanaya Okuda for helpful advice to conduct the kernel density estimation on the Python. We would like to thank Ryo Okumura, Hisao Yoshinaga, Yuto Iinuma for irradiation of dated samples at KUR, Institute for Integrated Radiation and Nuclear Science, Kyoto University. O.I. was supported by Grant-in-Aid (C) (No. 17K05686)) provided by JSPS.

References

1. Lay, T., Hernlund, J., & Buffett, B. A. (2008). Core–mantle boundary heat flow. *Nature Geoscience*, 1(1), 25-32.
2. Olson, P. L., Coe, R. S., Driscoll, P. E., Glatzmaier, G. A., & Roberts, P. H. (2010). Geodynamo reversal frequency and heterogeneous core–mantle boundary heat flow. *Physics of the Earth and Planetary Interiors*, 180(1-2), 66-79.
3. Ogg, J. G. (2020). Geomagnetic polarity time scale. Geologic time scale 2020, pp. 159–192, eds Gradstein, F.M., Elsevier.
4. McFadden, P. L. (1984). Statistical tools for the analysis of geomagnetic reversal sequences. *Journal of Geophysical Research: Solid Earth*, 89(B5), 3363-3372.
5. Buffett, B., & Avery, M. S. (2019). How Does Temporal Resolution Influence Geomagnetic Reversal Statistics?. *Geophysical Research Letters*, 46(10), 5146-5152.
6. Ahn, H. S., Kidane, T., Otofujii, Y., Yamamoto, Y., Ishikawa, N., & Yoshimura, Y. (2021). High-resolution palaeomagnetic results of Ethiopian trap series from Lima Limo section: implications for the Oligocene geomagnetic field behaviour and timing of volcanism. *Geophysical Journal International*, 225(1), 311-328.
7. Cande, S. C., & Kent, D. V. (1992). A new geomagnetic polarity time scale for the Late Cretaceous and Cenozoic. *Journal of Geophysical Research*, 97(B10), 13917-13951.
8. Rooney, T. O. (2017). The Cenozoic magmatism of East-Africa: Part I—Flood basalts and pulsed magmatism. *Lithos*, 286, 264-301.

9. Hofmann, C., Courtillot, V., Feraud, G., Rochette, P., Yirgu, G., Ketefo, E., & Pik, R. (1997). Timing of the Ethiopian flood basalt event and implications for plume birth and global change. *Nature*, 389(6653), 838-841.
10. Rochette, P., Tamrat, E., Féraud, G., Pik, R., Courtillot, V., Ketefo, E., Coulon, C., Hofmann, C., Vandamme, D., & Yirgu, G. (1998). Magnetostratigraphy and timing of the Oligocene Ethiopian traps. *Earth and Planetary Science Letters*, 164(3-4), 497-510.
11. Coulié, E., Quidelleur, X., Gillot, P. Y., Courtillot, V., Lefèvre, J. C., & Chiesa, S. (2003). Comparative K–Ar and Ar/Ar dating of Ethiopian and Yemenite Oligocene volcanism: implications for timing and duration of the Ethiopian traps. *Earth and Planetary Science Letters*, 206(3-4), 477-492.
12. Constable, C. (2000). On rates of occurrence of geomagnetic reversals. *Physics of the Earth and Planetary Interiors*, 118(3-4), 181-193.
13. Ishizuka, O., Uto, K., & Yuasa, M. (2003). Volcanic history of the back-arc region of the Izu-Bonin (Ogasawara) arc. *Geological Society, London, Special Publications*, 219(1), 187-205.
14. Yoshimura, Y., Yamazaki, T., Yamamoto, Y., Ahn, H. S., Kidane, T., & Otofujii, Y. (2020). Geomagnetic paleointensity around 30 Ma estimated from Afro-Arabian Large Igneous Province. *Geochemistry, Geophysics, Geosystems*, 21(12), e2020GC009341.
15. Kuiper, K. F., Deino, A., Hilgen, F. J., Krijgsman, W., Renne, P. R., & Wijbrans, A. J. (2008). Synchronizing rock clocks of Earth history. *Science*, 320(5875), 500-504.
16. Min, K., Mundil, R., Renne, P. R., & Ludwig, K. R. (2000). A test for systematic errors in $^{40}\text{Ar}/^{39}\text{Ar}$ geochronology through comparison with U/Pb analysis of a 1.1-Ga rhyolite. *Geochimica et Cosmochimica Acta*, 64(1), 73-98.
17. Vandamme, D. (1994). A new method to determine paleosecular variation. *Physics of the Earth and Planetary Interiors*, 85(1-2), 131-142.
18. Yamazaki, T., Yamamoto, Y., Acton, G., Guidry, E. P., & Richter, C. (2013). Rock-magnetic artifacts on long-term relative paleointensity variations in sediments. *Geochemistry, Geophysics, Geosystems*, 14(1), 29-43.
19. Yamamoto, Y., Yamazaki, T., Acton, G. D., Richter, C., Guidry, E. P., & Ohneiser, C. (2014). Palaeomagnetic study of IODP Sites U1331 and U1332 in the equatorial Pacific—extending relative geomagnetic palaeointensity observations through the Oligocene and into the Eocene. *Geophysical Journal International*, 196(2), 694-711.
20. Cox, A. (1968). Lengths of geomagnetic polarity intervals. *Journal of Geophysical Research*, 73(10), 3247-3260.

21. Shimazaki, H., & Shinomoto, S. (2010). Kernel bandwidth optimization in spike rate estimation. *Journal of computational neuroscience*, 29(1), 171-182.
22. Olson, P., & Amit, H. (2015). Mantle superplumes induce geomagnetic superchrons. *Frontiers in Earth Science*, 3, 38.
23. Hounslow, M. W., Domeier, M., & Biggin, A. J. (2018). Subduction flux modulates the geomagnetic polarity reversal rate. *Tectonophysics*, 742, 34-49.
24. Cande, S. C., & Kent, D. V. (1995). Revised calibration of the geomagnetic polarity timescale for the Late Cretaceous and Cenozoic. *Journal of Geophysical Research*, 100(B4), 6093-6095.
25. Huestis, S. P., & Acton, G. D. (1997). On the construction of geomagnetic timescales from non-prejudicial treatment of magnetic anomaly data from multiple ridges. *Geophysical Journal International*, 129(1), 176-182.
26. Ogg, J. G., Ogg, G. M., & Gradstein, F. M. (2016). A concise geologic time scale: 2016.
27. Tejada, M. L. G., Geldmacher, J., Hauff, F., Heaton, D., Koppers, A. A., Garbe-Schönberg, D., Hoernle, K., Heydolph, K., & Sager, W. W. (2016). Geochemistry and age of Shatsky, Hess, and Ojin Rise seamounts: Implications for a connection between the Shatsky and Hess Rises. *Geochimica et Cosmochimica Acta*, 185, 302-327.
28. Gomes, A. S., & Vasconcelos, P. M. (2021). Geochronology of the Paraná-Etendeka large igneous province. *Earth-Science Reviews*, 103716.
29. Timm, C., Hoernle, K., Werner, R., Hauff, F., van den Bogaard, P., Michael, P., Coffin, M., & Koppers, A. (2011). Age and geochemistry of the oceanic Manihiki Plateau, SW Pacific: New evidence for a plume origin. *Earth and Planetary Science Letters*, 304(1-2), 135-146.
30. Jiang, Q., Jourdan, F., Olierook, H. K., Merle, R. E., & Whittaker, J. M. (2021). Longest continuously erupting large igneous province driven by plume-ridge interaction. *Geology*, 49(2), 206-210.
31. Serrano, L., Ferrari, L., Martínez, M. L., Petrone, C. M., & Jaramillo, C. (2011). An integrative geologic, geochronologic and geochemical study of Gorgona Island, Colombia: Implications for the formation of the Caribbean Large Igneous Province. *Earth and Planetary Science Letters*, 309(3-4), 324-336.
32. Schoene, B., Eddy, M. P., Samperton, K. M., Keller, C. B., Keller, G., Adatte, T., & Khadri, S. F. (2019). U-Pb constraints on pulsed eruption of the Deccan Traps across the end-Cretaceous mass extinction. *Science*, 363(6429), 862-866.
33. Storey, M., Duncan, R. A., & Tegner, C. (2007). Timing and duration of volcanism in the North Atlantic Igneous Province: Implications for geodynamics and links to the Iceland hotspot. *Chemical Geology*, 241(3-4), 264-281.

34. Kasbohm, J., & Schoene, B. (2018). Rapid eruption of the Columbia River flood basalt and correlation with the mid-Miocene climate optimum. *Science Advances*, 4(9), eaat8223.

Online Methods

$^{40}\text{Ar}/^{39}\text{Ar}$ dating

Ages of the basalt samples from the Lima-Limo section were determined using the $^{40}\text{Ar}/^{39}\text{Ar}$ dating instrument at the Geological Survey of Japan/AIST. Details of the procedures are described in Ishizuka et al. (13). 20-25 mg of phenocryst-free groundmass, crushed and sieved to 250-500 μm in size, was analyzed using a step-wise heating procedure. The samples were treated in 6N HCl for 30 minutes and then 4N HNO_3 for 30 minutes at 95°C with stirring to remove any alteration products (clays and carbonates) present in interstitial spaces. After this treatment, samples were examined under a microscope, and microphenocrysts of clinopyroxene were removed. This procedure effectively separated and concentrated fresh plagioclase in the groundmass and microphenocrysts. Sample irradiation was done at the reactor of the Institute for Integrated Radiation and Nuclear Science, Kyoto University for four hours. Sanidine separated from the Fish Canyon Tuff (FC3) was used for the flux monitor and assigned an age of 27.5 Ma, which has been determined against our primary standard for our K-Ar laboratory³⁵, Sori biotite, whose age is 91.2 Ma.

A CO_2 laser heating system (NEWWAVE MIR10-30) was used at continuous wave mode for sample heating. A faceted lens was used to obtain a 3.2 mm-diameter beam with homogenous energy distribution to ensure uniform heating of the samples during stepwise heating analysis. Argon isotopes were measured on a IsotopX NGX noble gas mass spectrometer fitted with a Hamamatsu Photonics R4146 secondary electron multiplier in a peak-jumping mode.

Correction for interfering isotopes was achieved by analyses of CaF_2 and KFeSiO_4 glasses irradiated with the samples. The blank of the system including the mass spectrometer and the extraction line was 2.9×10^{-14} ml STP for ^{36}Ar , 1.4×10^{-13} ml STP for ^{37}Ar , 1.0×10^{-14} ml STP for ^{38}Ar , 1.2×10^{-14} ml STP for ^{39}Ar and 1.9×10^{-12} ml STP for ^{40}Ar . The blank analysis was done every two or three step analyses. All errors for $^{40}\text{Ar}/^{39}\text{Ar}$ results are reported at one standard deviation. Errors for ages include analytical uncertainties for Ar isotope analysis, correction for interfering isotopes and J value estimation. An error of 0.5% was assigned to J values as a pooled estimate during the course of this study. Results of Ar isotopic analyses and correction factors for interfering isotopes are presented in supplementary data (Table S1).

Plateau ages were calculated as weighted means of ages of plateau-forming steps, where each age was weighted by the inverse of its variance. The age plateaus were determined following the definition³⁶. Inverse isochrons were calculated using York's least-squares fit³⁷, which accommodates errors in both ratios and correlations of errors.

Geomagnetic reversal frequency calculation

The relative geomagnetic reversal frequency variations were computed in Python 3.7.3 using the `sskernel.py` function for the fixed KDE and the `ssvkernel.py` function for the locally adaptive KDE. The methods are the Kernel Bandwidth optimization approach¹⁸ with a Gaussian window function (<https://pypi.org/project/adaptivekde/>). The relative geomagnetic reversal frequency was converted to an absolute value using the average reversal frequency over the past 154.9 Ma calculated from GPTS2020. The only assumption of both methods is that the data are generated from a Poisson process. On the locally adaptive KDE, optimized bandwidths are determined locally based on minimization of the mean integrated square error between the unknown underlying rate and the estimated rate.

Methods References

35. Uchiumi, S., & Shibata, K. (1980). Errors in K-Ar age determination. *Bulletin of Geological Survey of Japan*, 31(6), 267-273.

36. Fleck, R. J., Sutter, J. F., & Elliot, D. H. (1977). Interpretation of discordant $^{40}\text{Ar}/^{39}\text{Ar}$ age-spectra of Mesozoic tholeiites from Antarctica. *Geochimica et Cosmochimica Acta*, 41(1), 15-32.

37. York, D. (1968). Least squares fitting of a straight line with correlated errors. *Earth and planetary science letters*, 5, 320-324.

Table 1

Table 1 is available in the Supplementary Files section.

Figures

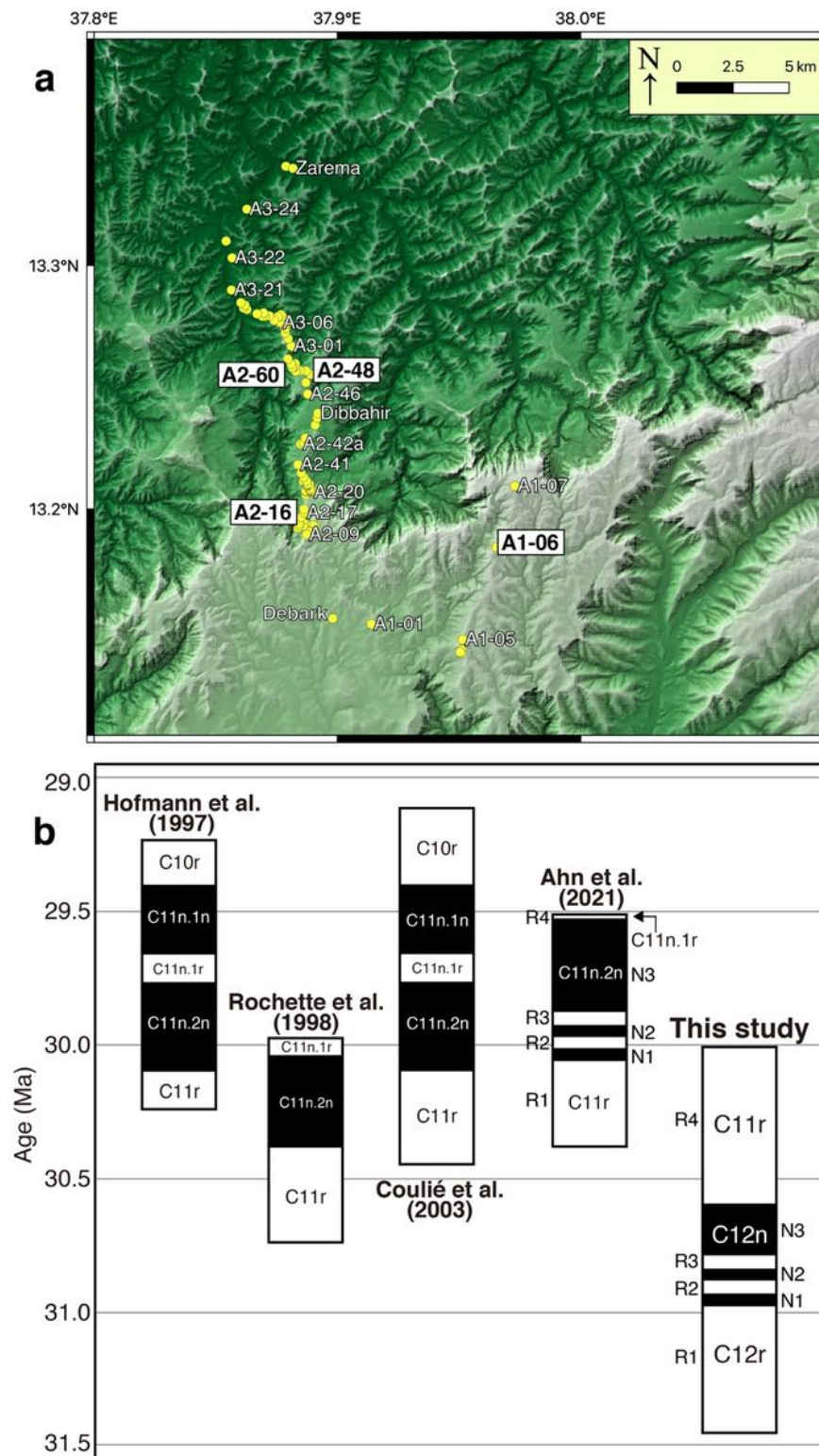


Figure 1

(a) Map of the sampling sites (yellow circles) in the Lima-Limo section. Black letters show lava flows used for $^{40}\text{Ar}/^{39}\text{Ar}$ dating in this study. (b) Summary of previous and our magnetostratigraphic correlations of the Lima-Limo section. The reference GPTS used are Cande and Kent (24) for Hofmann et al. (8), Huestis & Acton (25) for Rochette et al. (9), Cande and Kent (24) for Coulié et al. (10), Ogg et al. (26) for Ahn et al. (6), and Ogg (3) for this study. When multiple age correlations were proposed in the

previous studies, only the correlations preferred by the original authors in each study is presented here. We assumed that the Lima-Limo reversals are evenly distributed over the early half of Chron C12n.

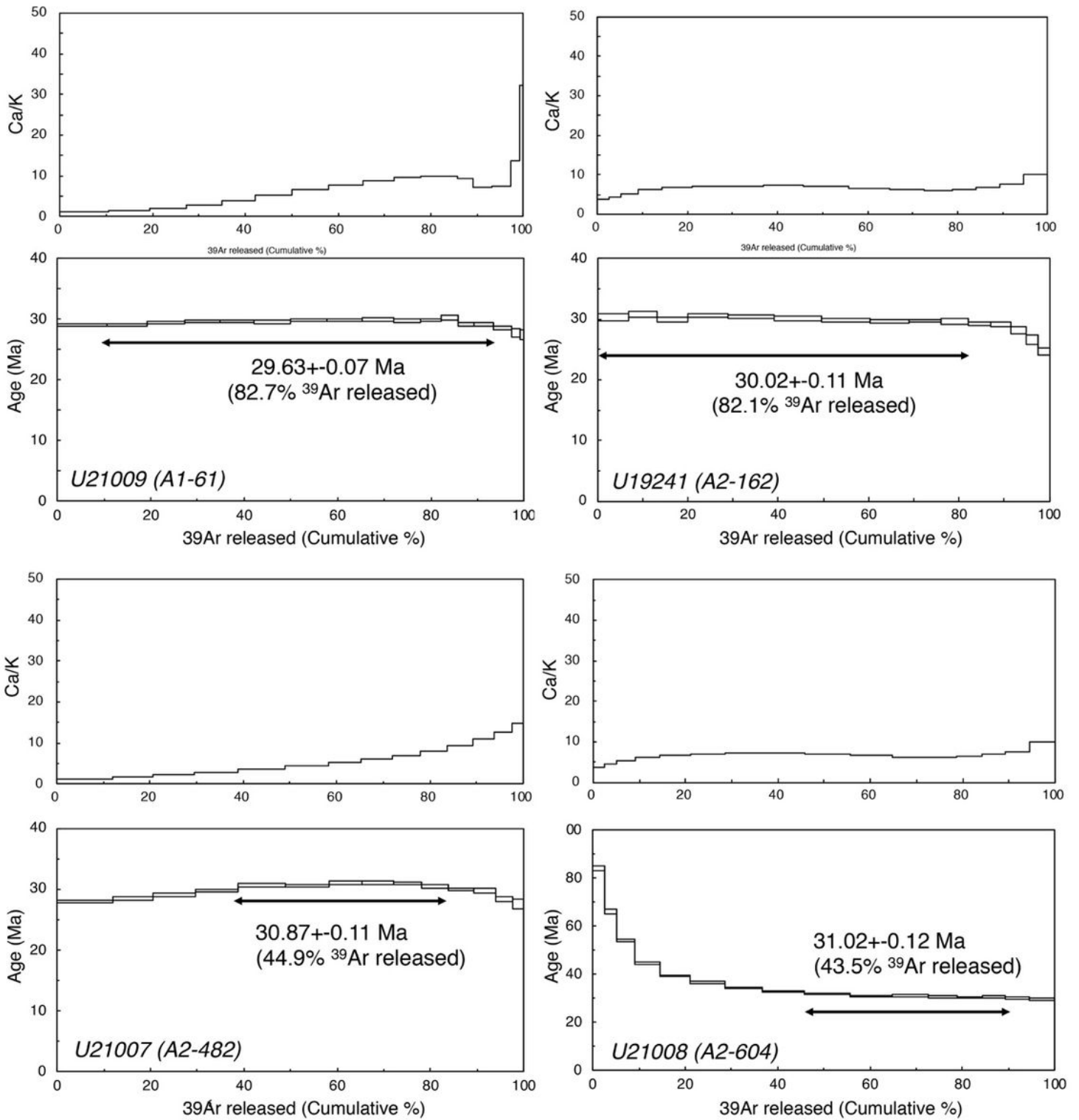


Figure 2

$^{40}\text{Ar}/^{39}\text{Ar}$ age spectra and Ca/K plots for leached groundmass samples. Arrows indicate the steps forming plateau ages. $^{40}\text{Ar}/^{39}\text{Ar}$ plateau ages are shown with 1σ error.

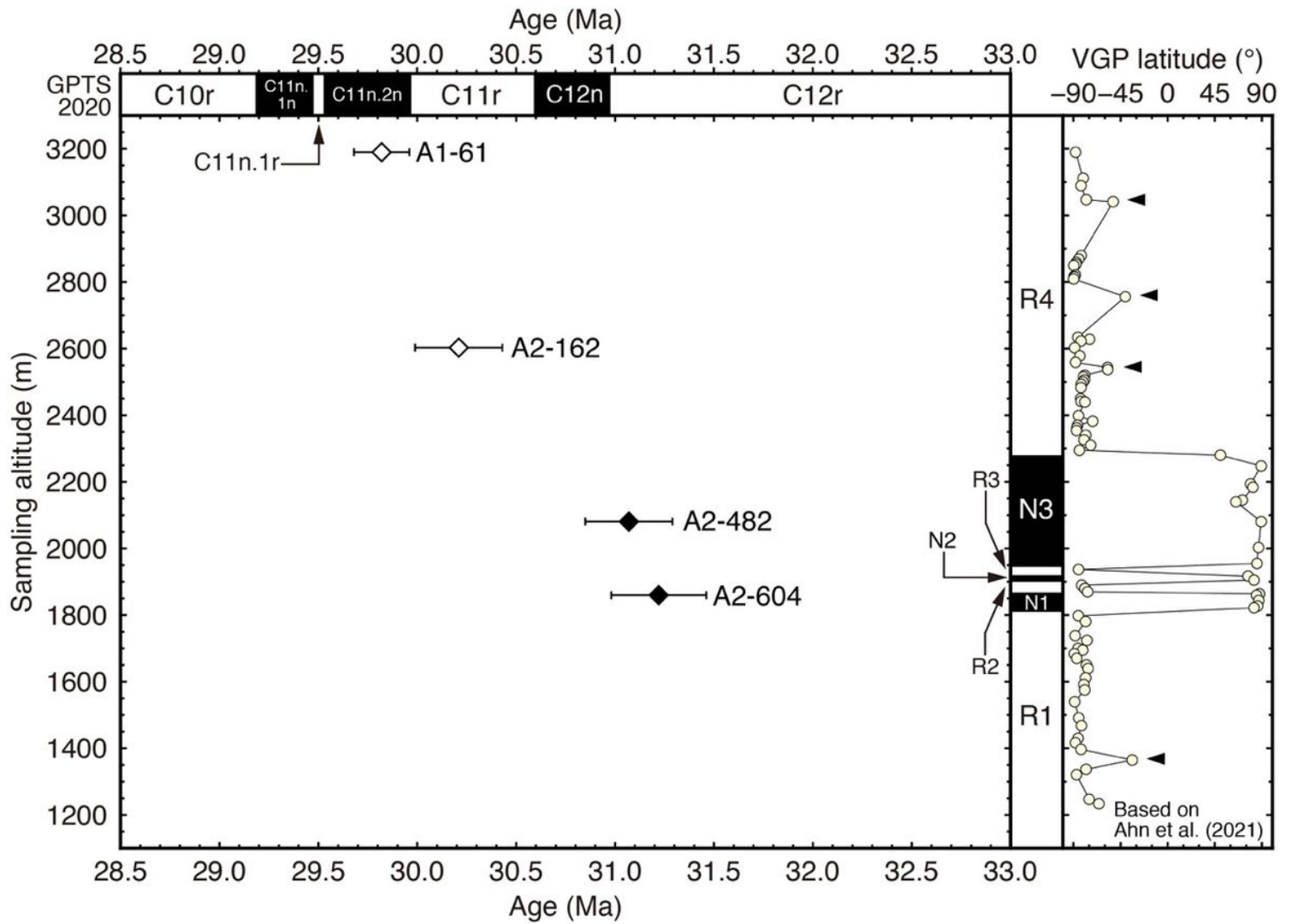


Figure 3

Comparison of our $^{40}\text{Ar}/^{39}\text{Ar}$ ages from the Lima-Limo section with GPTS2020³. The latest magnetostratigraphy and VGP latitudes for the Lima-Limo section⁶ is shown on the right-hand side, where reverse (normal) magnetozones are filled by white (black). The VGP latitudes are corrected by African plate motion with their palaeomagnetic pole by Yoshimura et al. (13). The black triangles indicate putative excursions identified by Ahn et al. (6). All ages are recalibrated to the FCs standard with an age of 28.201 Ma¹⁴ and the ^{40}K decay constant¹⁵, which are used in GPTS2020. The $^{40}\text{Ar}/^{39}\text{Ar}$ ages obtained in this study are shown with 2σ error.

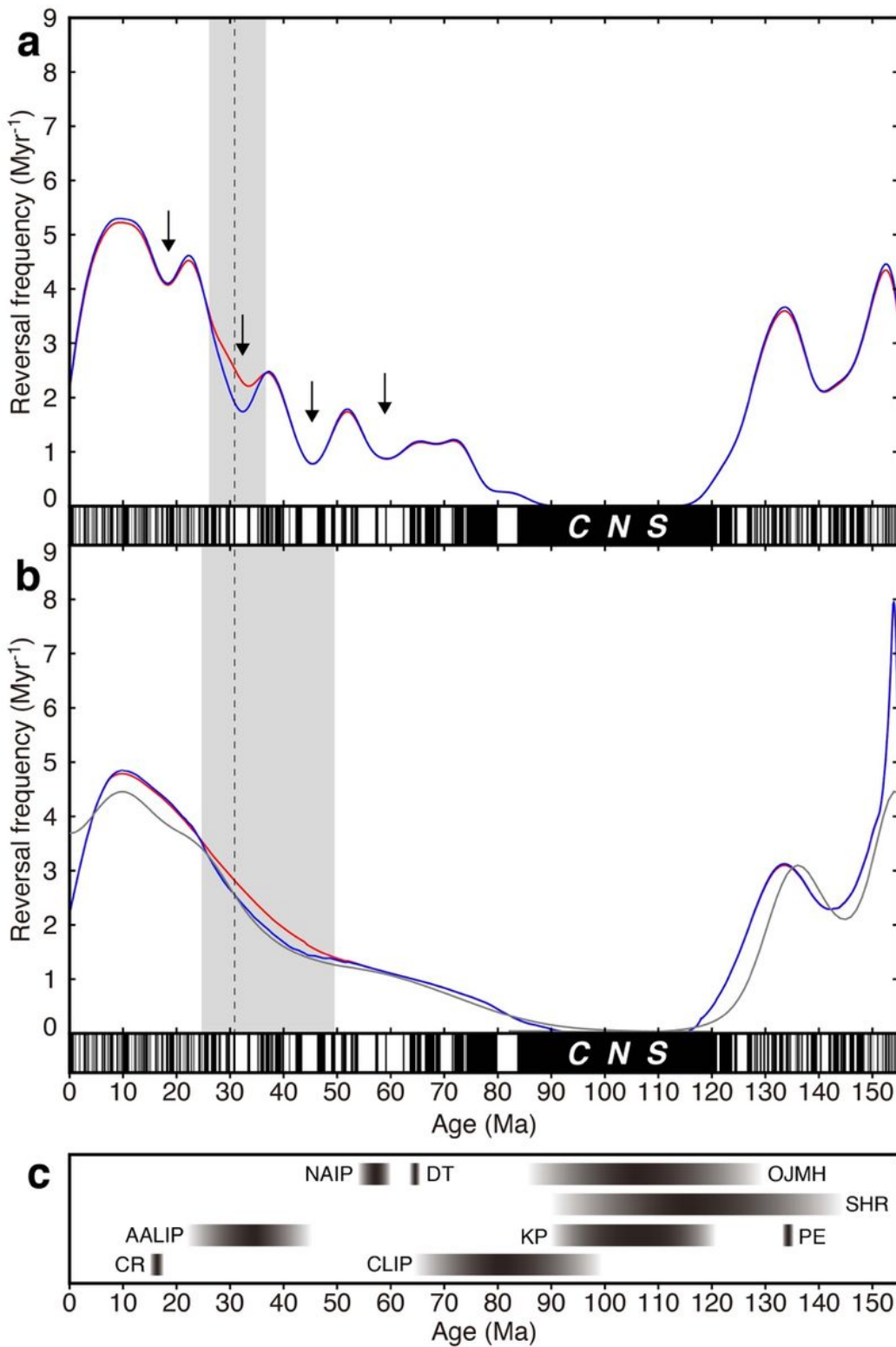


Figure 4

(a) Reversal frequency curves since 154.9 Ma for GPTS2020³ based on the fixed kernel density estimation, before and after adding the newly found four reversals (the Lima-Limo reversals) to Chron C12n based on GPTS2020 (solid blue and red line, respectively). The bandwidth of the fixed KDE before and after adding the new reversals are 2.551 and 2.619, respectively. Arrows indicate minima of the reversal frequency. The normal/reverse polarities of GPTS2020 are shown as black/white bars, which do

not include the Lima-Limo reversals. The dashed black line shows the timing of the Lima-Limo reversals in Chron C12n. Gray area indicates intervals when the curve has changed significantly by adding the Lima-Limo reversals. We assumed that the Lima-Limo reversals are evenly distributed over the early half of Chron C12n. (b) Reversal frequency curves based on locally adaptive kernel density estimation, before and after adding the Lima-Limo reversals to Chron C12n (solid blue and red line, respectively). (c) Ages of LIPs activity after 154.9 Ma (SHR: Shatsky-Hess Rise, Tejada et al. (27); PE: Paraná-Etendeka Large Igneous Province, Gomes and Vasconcelos (28); OJMH: Ontong Java, Manihiki, and Hikurangi Plateaus, Timm et al. (29); KP: Kerguelen Plateau, Jiang et al. (30); CLIP, Serrano et al. (31); DT; Deccan Traps, Schoene et al. (32); NAIP: North Atlantic Igneous Province, Storey et al. (33); AALIP: Afro-Arabian Large Igneous Province, Rooney (7); CR: Columbia River flood basalt, Kasbohm and Schoene (34)).

Supplementary Files

This is a list of supplementary files associated with this preprint. Click to download.

- [LLchrontable1.xlsx](#)
- [LLchrontableS1.xlsx](#)
- [LLchrontableS2.xlsx](#)
- [floatimage6.jpeg](#)
- [floatimage7.jpeg](#)
- [floatimage8.jpeg](#)